OEA | Opto-Electronic Advances

Article

January 2026, Vol. 9, No. 1

Open Access

High-fidelity full-color self-interference incoherent digital holography via quarter-wave geometric phase optics

Jae-Won Lee[1], Jin-Hyeok Seo[1], Jung-Yeop Shin[1], Jing-Wen Bu[1], Kihong Choi[2], Keehoon Hong[2] and Hak-Rin Kim[1,3]*

Abstract: We present a compact self-interference incoherent digital holography (SIDH) system that incorporates a quarter-waveplate (QWP)-based geometric phase (GP) lens to achieve high-fidelity, full-color holographic imaging under broadband incoherent illumination. Traditional SIDH systems that utilize half-waveplate (HWP)-based GP lenses are hindered by unavoidable triple-wavefront polarization interference, stemming from chromatic dispersion in phase retardation. This interference introduces color-dependent artifacts in the reconstructed images. In contrast, our QWP-based design inherently suppresses such interference by using the non-diffracted beam as the reference, enabling stable dual-wavefront modulation. This approach produces phase-encoded polarization interference patterns that remain spectrally consistent across the red, green, and blue (RGB) channels. Experimental results demonstrate substantial noise suppression and significantly improved full-color image fidelity, supported by channel-specific noise analysis and structural similarity metrics. The system also preserves a simplified optical configuration without active polarization control, allowing for compact integration and cost-effective fabrication. These advantages position the proposed QWP-GP SIDH architecture as a promising solution for portable, real-time digital holographic 3D imaging, with scalable potential in applications such as augmented reality, optical diagnostics, and spectral holography.

Keywords: self-interference incoherent digital holography; digital holography; geometric phase lens; polarization interference; holographic imaging

DOI: 10.29026/oea.2026.250149 | CSTR: 32247.14.oea.2026.250149

Citation: Lee JW, Seo JH, Shin JY et al. High-fidelity full-color self-interference incoherent digital holography via quarter-wave geometric phase optics. *Opto-Electron Adv* **9**, 250149 (2026).

1 Introduction

Digital holography (DH) is a computational imaging technique that captures and reconstructs the complete complex optical wavefront —including both amplitude and phase —using intensity-only measurements. By recording interference fringe patterns between the object and reference beams on a single sensor plane, DH enables powerful capabilities such as digital refocusing, depth-resolved phase retrieval, and high-precision 3D imaging[1,2]. These advantages have driven the widespread applications in biomedical diagnostics, extended reality (XR), and optical metrology[3–5].

In parallel with DH, lensless imaging strategies have recently advanced high-resolution and quantitative phase imaging by integrating diffraction control or programmable apertures with computational reconstruction. Notable examples include holography-based quantitative phase imaging, palm-sized single-shot full-color incoherent holographic cameras under white light, programmable or complex Fresnel zone aperture designs, lensless cameras engineered with point spread function control, as well as polarization-multiplexed multichannel holography and multi-foci metalenses for spectral and polarization-ellipticity recognition[6–12]. Within this broader landscape, self-interference incoherent digital holography (SIDH) has emerged as a particularly promising approach for use under ambient lighting conditions or in scenarios where bulky and

Received: 13 June 2025

Accepted: 16 November 2025

Published online: 27 January 2026

[1]School of Electronic and Electrical Engineering, Kyungpook National University, Daegu 41566, Republic of Korea; [2]Digital Holography Research Section, Electronics and Telecommunications Research Institute, Daejeon 34129, Republic of Korea; [3]School of Electronics Engineering, Kyungpook National University, Daegu 41566, Republic of Korea.
*Correspondence: HR Kim, E-mail: rineey@knu.ac.kr

expensive coherent light sources are impractical[13–15]. Unlike traditional two-path interferometry, SIDH generates interference patterns via in-line wavefront division, enabling compact, robust, and vibration-insensitive optical systems that are well ideally suited for portable or real-time 3D holographic imaging platforms.

To this end, wavefront modulation using geometric phase (GP) optics—particularly GP lenses—has recently become a compelling strategy for implementing SIDH systems[16–21]. Unlike conventional phase control methods that rely on active spatial light modulators or multilayer diffractive structures[22,23], GP lenses exploit spatially varying birefringent optic axis modulation to introduce polarization-selective conjugate quadratic phase distributions. This enables ultrathin, polarization-sensitive wavefront shaping through the Pancharatnam-Berry phase[24], a geometric phase that arises from the evolution of the polarization state on the Poincaré sphere rather than from differences in optical path length[25].

In half-waveplate (HWP)-based GP lenses, linearly polarized incident light is decomposed into left-handed circularly polarized (LCP) and right-handed circularly polarized (RCP) components, each acquiring an opposite spatially varying phase[26–28]. This results in the generation of symmetric ±1st-order diffracted beams that encode the object's phase into polarization-dependent interference patterns. This passive and compact approach enables high-fidelity wavefront control without the need for complex electronics or bulky optical components[18,29]. As a result, GP-SIDH systems offer scalable, alignment-tolerant architectures ideal for miniaturized 3D imaging applications.

These features have accelerated the development of GP-SIDH technologies. For instance, pixel-divided polarization-sensitive image sensors have enabled real-time acquisition of phase-encoded polarization interference maps using phase-shifting schemes within a compact form factor[18,19]. More recently, temporal multiplexing of GP phase shifts using high-speed polarization modulators has further enhanced spatial resolution and optical flexibility, while remaining compatible with standard imaging sensors. Collectively, these advances are pushing GP-SIDH toward practical deployment in high-speed, high-resolution, and miniaturized holographic imaging systems[20].

However, despite these promising developments, achieving high-fidelity full-color imaging with conventional HWP-based GP-SIDH systems remains fundamentally challenging. The wavelength-dependent birefringence of GP materials leads to deviations from the ideal π phase retardation condition, resulting in incomplete ±1st-order diffraction and leakage of the residual 0th-order beam. This residual component acts as an unintended third wavefront, introducing triple-wavefront interference that degrades the desired two-beam polarization interference and introduces holographic noise[30–32]. Critically, such noise cannot be fully suppressed during holographic reconstruction using conventional phase-shifting techniques, leading to persistent spectral artifacts—particularly under broadband or RGB illumination[19]. These limitations have significantly hindered the imaging fidelity and practical implementation of full-color GP-SIDH systems, motivating the development of alternative strategies to inherently suppress unwanted wavefront interference while retaining the core benefits of GP-based modulation.

2 Results

2.1 Full-color SIDH imaging via QWP-based GP lens

To address the inherent spectral limitations of conventional HWP-based GP optics in full-color SIDH systems, we propose a compact holographic imaging architecture that integrates a QWP-based GP lens, as illustrated in Fig. 1. By precisely engineering both the incident polarization state and the GP phase retardation condition, the system inherently suppresses the undesired third wavefront component. This enables stable two-beam self-interference across the full RGB spectrum, eliminating the need for additional numerical denoising.

This section presents the optical principles and polarization interference characteristics of the proposed QWP-GP SIDH configuration, with direct comparisons to its HWP-based counterpart under broadband incoherent illumination. We analyze the wavelength-dependent behavior of wavefront modulation, simulate the formation of phase-encoded polarization interference patterns, and assess the impact of chromatic retardation variation on reconstruction quality using a phase-shifting technique. These theoretical findings are experimentally validated through comparative measurements of GP diffraction efficiency and full-color holographic image reconstructions.

Our results demonstrate that the QWP-GP lens design effectively eliminates triple-wavefront interference, a persistent limitation in full-color GP-SIDH systems. The design substantially improves RGB reconstruction fidelity, marking a significant advancement toward practical, high-quality incoherent digital holography.

2.2 Comparative simulation of HWP- and QWP-based GP-SIDH configurations

In a GP-SIDH system, the GP lens modulates both the phase and polarization state of the incident beam, as described by Eq. (1):

$$e^{i\delta_{in}}\left|\chi_{in}\right\rangle^{GP} \rightarrow \sqrt{\eta_+}e^{i(\delta_{in}-\Phi)}\left|\chi_+\right\rangle + \sqrt{\eta_-}e^{i(\delta_{in}+\Phi)}\left|\chi_-\right\rangle + \sqrt{\eta_0}e^{i\delta_{in}}\left|\chi_{in}\right\rangle , \tag{1}$$

where δ_{in} is the initial phase of the incident beam, and Φ is the convex lens phase profile recorded onto the GP lens. The polarization states $|\chi_{in}\rangle$, $|\chi_+\rangle$, and $|\chi_-\rangle$ correspond, respectively, to the incident (or undiffracted) polarization state and

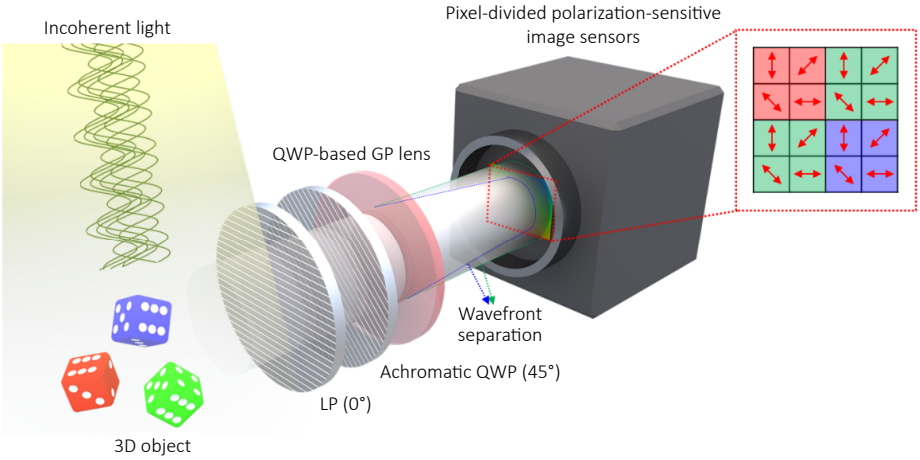


Fig. 1 | Schematic of the SIDH system employing a quarter-waveplate (QWP)-based GP lens. The setup includes a polarization-sensitive image sensor to capture real-time interference patterns generated between the non-diffracted 0th-order reference beam and the 1st-order object beam. The QWP-GP SIDH configuration enables dual wavefront modulation for generating phase-encoded polarization interference maps, while maintaining compatibility with broadband incoherent illumination.

the ±1st-order diffracted components associated with RCP and LCP.

The spatially varying phase modulation $\Phi(x, y) = 2\theta_{\mathrm{bi}}(x, y)$ rises from the spatially varying birefringent optic axis orientation $\theta_{\mathrm{bi}}(x, y)$ of the GP lens. This modulation follows the Pancharatnam-Berry phase principle[17,26,28], where geometric phase is imparted through local changes in the optic axis rather than physical thickness. The phase retardation Γ introduced by the GP lens depends on the material and structural parameters of reactive mesogen (RM) layer and is given by:

$$\Gamma = \frac{2\pi\Delta n d}{\lambda}\ , \tag{2}$$

where Δn is the birefringence of the RM material, d is the thickness of the RM layer, and λ is the wavelength of the incident light. This phase retardation directly determines the efficiency of GP wavefront modulation efficiency[33,34]. The efficiency of the undiffracted 0th-order beam is:

$$\eta_0 = \cos^2\left(\frac{\Gamma}{2}\right)\ , \tag{3}$$

indicating that when $\Gamma \neq \pi$, part of the input light remains in the 0th-order component without undergoing GP modulation. The ±1st-order diffraction efficiencies are given by:

$$\eta_{\pm 1} = \frac{1}{2}\left[1 \mp S_3'\right]\sin^2\left(\frac{\Gamma}{2}\right)\ , \tag{4}$$

where S_3' is the third Stokes parameter, representing the degree of circular polarization of the input beam. These expressions collectively describe how the GP lens redistributes the input beam into various diffraction orders based on polarization state and wavelength.

In a conventional HWP-based GP lens, the phase retardation Γ is ideally designed to be π, ensuring that for a circularly polarized input ($S_3' = \pm 1$), Eq. (4) yields $\eta_{\pm 1} = 1$, meaning the entire beam is diffracted into a single ±1st-order component with opposite handedness. In typical GP-SIDH systems, linearly polarized light ($S_3' = 0$) is used, which is equally decomposed into orthogonal LCP and RCP components after passing through the HWP-based GP lens. These components acquire opposite GP and are diffracted into ±1st-order beams. Their self-interference forms phase-encoded polarization patterns, which are subsequently reconstructed into phase maps via SIDH.

In practice, especially under full-color or ambient illumination, the birefringent RM materials used in GP lenses exhibit chromatic dispersion, as described by Eq. (2). While the GP lens can be optimized for $\Gamma = \pi$ at a target wavelength, deviations are unavoidable at other wavelengths. These spectral deviations reduce the GP modulation efficiency, leading to incomplete transfer of energy into the ±1st-order beams. According to Eq. (3), this causes a non-zero η_0 component, introducing a residual undiffracted 0th-order beam.

As illustrated in Fig. 2(a), this 0th-order component acts as a third, unintended wavefront, giving rise to triple-wavefront interference. This deviation from ideal two-beam interference introduces phase noise and significantly degrades holographic image quality, especially across the RGB spectrum in full-color DH[35]. The effects of this unwanted component, and its polarization-dependent interference behavior, will be further investigated through phase-encoded polarization-based SIDH simulations in the following sections.

To overcome the limitations of the HWP-based GP-SIDH system, we propose a QWP-based GP-SIDH configuration, where the GP lens is designed with a phase retardation of $\Gamma = \pi/2$, as illustrated in Figs. 1 and 2(b). Unlike the HWP-

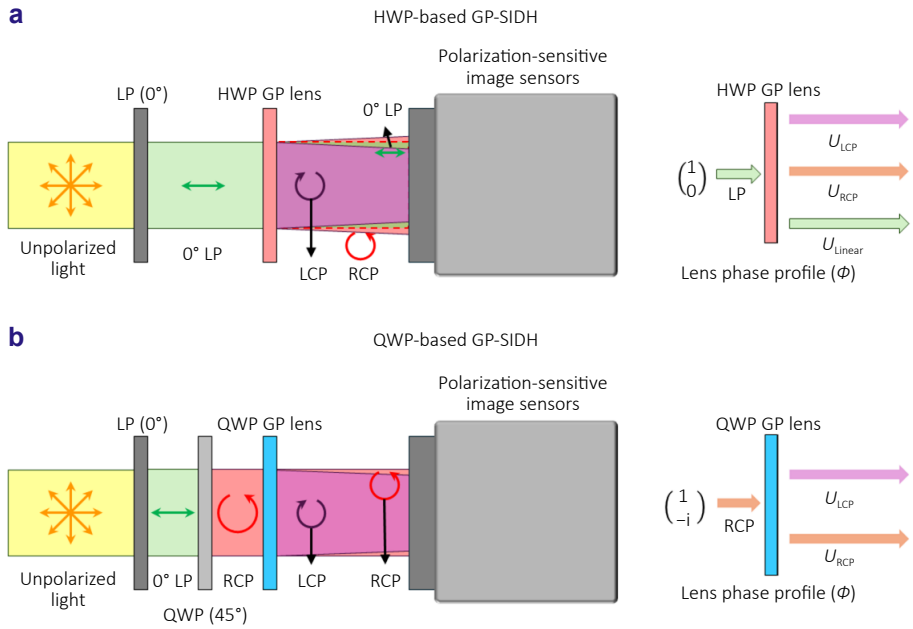


Fig. 2 | Schematic comparison of in-line wavefront separation in GP-SIDH systems using HWP-based and QWP-based configurations. (a) In the HWP-based setup, a linearly polarized beam passes through a GP lens with π phase retardation, generating symmetric ±1st-order diffracted beams along with a residual 0th-order leakage due to chromatic dispersion, leading to triple-wavefront interference. (b) In the QWP-based setup, the input beam is first converted to circular polarization before passing through a GP lens with π/2 phase retardation, producing only the 0th- and +1st- or −1st-order wavefronts, thereby inherently eliminating triple-wavefront interference.

based setup shown in Fig. 2(a)—where linearly polarized light is decomposed into ±1st-order diffracted beams, the QWP-based system utilizes a circularly polarized input ($S_3' = \pm 1$), resulting in a fundamentally different wavefront separation mechanism[36]. Under this condition, the transmitted light consists only of the 0th-order and one of the ±1st-order diffraction components, thereby intrinsically suppressing triple-wavefront interference.

Substituting $\Gamma = \pi/2$ and $S_3' = \pm 1$ into Eqs. (3) and (4), we find $\eta_0 = 0.5$ and $\eta_{\pm 1} = 0.5$, indicating that the optical power is equally distributed between the 0th- and ±1st-order beams under ideal conditions. Although fabrication imperfections or chromatic dispersion may cause deviations from the target retardation $\Gamma = \pi/2$, such deviations only affect the relative amplitudes of the two beams. Crucially, no additional diffracted component is generated, and the two-beam interference condition required for SIDH remains intact.

This concept is schematically illustrated in Fig. 2, which contrasts the wavefront separation mechanisms of HWP- and QWP-based GP-SIDH systems. In the HWP case, deviations from the ideal retardation value at different wavelengths introduce a residual 0th-order beam, resulting in a third interfering wavefront that severely degrades image quality. In contrast, the QWP configuration inherently suppresses this residual component, maintaining a clean two-beam interference condition regardless of wavelength. While chromatic dispersion still affects the amplitude ratio between the 0th- and ±1st-order beams, it does not introduce additional spectral artifacts or compromise phase fidelity. Consequently, the QWP-based system reliably produces high-quality, phase-encoded self-interference patterns across the entire RGB spectrum under broadband illumination.

To better understand the limitations of the conventional HWP-based GP-SIDH and highlight the advantages of the proposed QWP-based design, we theoretically analyze the effects of triple-wavefront interference. The total wavefront formed in GP-SIDH can be expressed by Eqs. (5–7), where U_{LCP} and U_{RCP} denote the LCP and RCP beams, and U_{DC} corresponds to the unmodulated direct current (DC) component, respectively. The terms $\sqrt{\eta_{+1}}$, $\sqrt{\eta_{-1}}$, and $\sqrt{\eta_0}$ represent the amplitude coefficients of the +1st-order, −1st-order, and 0th-order beams, respectively, as determined by the GP lens's polarization-dependent diffraction efficiency. The GP lens phase profile $\Phi(x, y)$ modulates the wavefronts as follows:

$$U_{\mathrm{LCP}} = A_{\mathrm{o}}(x,y)\sqrt{\eta_{+1}}\mathrm{e}^{\mathrm{i}\Phi_{\mathrm{o}}(x,y)}\mathrm{e}^{+\mathrm{i}\Phi(x,y)}, \tag{5}$$

$$U_{\mathrm{RCP}} = A_{\mathrm{o}}(x,y)\sqrt{\eta_{-1}}\mathrm{e}^{\mathrm{i}\Phi_{\mathrm{o}}(x,y)}\mathrm{e}^{-\mathrm{i}\Phi(x,y)}, \tag{6}$$

$$U_{\mathrm{DC}} = A_{\mathrm{o}}\sqrt{\eta_0}(x,y)\,\mathrm{e}^{\mathrm{i}\Phi_{\mathrm{o}}(x,y)}, \tag{7}$$

where, $A_{\mathrm{O}}(x, y)$ and $\Phi_{\mathrm{O}}(x, y)$ represent the amplitude and phase of object wavefront. In the HWP-based GP-SIDH, the modulated wavefront passes through a linear polarizer (LP) oriented at angle θ_{LP}. The corresponding components of the total wavefront, and the overall intensity I_θ are given by:

$$U^{\theta_{\rm LP}}_{\rm H,LCP} = \frac{1}{\sqrt{2}} U_{\rm LCP} \cdot (\cos\theta_{\rm LP} + {\rm i}\sin\theta_{\rm LP}) \ , \tag{8}$$

$$U^{\theta_{\rm LP}}_{\rm H,RCP} = \frac{1}{\sqrt{2}} U_{\rm RCP} \cdot (\cos\theta_{\rm LP} - {\rm i}\sin\theta_{\rm LP}) \ , \tag{9}$$

$$U^{\theta_{\rm LP}}_{\rm H,DC} = U_{\rm DC} \cdot \cos\theta_{\rm LP} \ , \tag{10}$$

$$I_{{\rm H},\theta} = \left|U^{\theta_{\rm LP}}_{\rm H,Total}\right|^2 = \left|U^{\theta_{\rm LP}}_{\rm H,LCP} + U^{\theta_{\rm LP}}_{\rm H,RCP} + U^{\theta_{\rm LP}}_{\rm H,DC}\right|^2 . \tag{11}$$

To reconstruct the complex hologram using the four-phase shifting technique, intensity measurements I_0, I_{45}, I_{90}, and I_{135} are recorded at LP angles of 0°, 45°, 90°, and 135°, respectively[37,38]. Based on Eqs. (8–11), the real and imaginary components of the product $U_{\rm LCP}U^*_{\rm RCP}$ can be extracted as:

$$\begin{aligned}\frac{I_0 - I_{90}}{2} =& {\rm Re}\left(U_{\rm LCP}U^*_{\rm RCP}\right) + \frac{1}{2}|U_{\rm DC}|^2 \\ &+ \frac{\sqrt{2}}{2}{\rm Re}\left(U_{\rm DC}\left(U^*_{\rm LCP} + U^*_{\rm RCP}\right)\right) \ ,\end{aligned} \tag{12}$$

$$\frac{I_{45} - I_{135}}{2} = {\rm Im}\left(U_{\rm LCP}U^*_{\rm RCP}\right) - \frac{\sqrt{2}}{2}{\rm Im}\left(U_{\rm DC}U^*_{\rm RCP}\right) \ . \tag{13}$$

These expressions reveal how the unwanted DC component in the HWP-based system corrupts the ideal interference pattern. In contrast, the QWP-based approach eliminates unwanted component, enabling clean two-beam interference for high-fidelity holographic reconstruction under full-color, broadband illumination.

In contrast, the proposed QWP-based GP-SIDH system utilizes a phase retardation of $\Gamma = \pi/2$ and a circularly polarized input beam ($S'_3 = \pm 1$). Under these conditions, the diffraction efficiencies become $\eta_0 = \eta_{\pm 1} = 0.5$, ensuring that only two coherent beams are generated. These beams—0$^{\rm th}$- and ±1$^{\rm st}$-order—interfere to form the hologram without introducing a third interfering component. Even if Γ deviates due to fabrication errors or dispersion, the total wavefront remains confined to two components, with only their intensity ratio changing. This dual-beam configuration inherently prevents triple-wavefront interference, ensuring robust phase-shifting-based reconstruction even under broadband illumination.

For instance, when the incident light is RCP ($S'_3 = +1$), the output comprises the 0$^{\rm th}$-order wavefront $U_{\rm DC}$, which retains its incident RCP state, and the 1$^{\rm st}$-order modulated wavefront $U_{\rm LCP}$, which is converted to the opposite LCP state. These two components interfere after transmission through a LP oriented at angle $\theta_{\rm LP}$, applying phase-shifting in the GP-SIDH system. This interference produces an intensity distribution governed by Eq. (14) and (15) and a total wavefront intensity described by Eq. (16). In this dual-beam configuration, no residual third wavefront is present, allowing the real and imaginary components of the complex hologram $U_{\rm LCP}U^*_{\rm DC}$ to be accurately reconstructed using the four-phase shifting method. As a result, twin-image and bias noise are effectively suppressed.

$$U^{\theta_{\rm LP}}_{\rm Q,LCP} = \frac{1}{\sqrt{2}} U_{\rm LCP} \cdot (\cos\theta_{\rm LP} + {\rm i}\sin\theta_{\rm LP}) \ , \tag{14}$$

$$U^{\theta_{\rm LP}}_{\rm Q,RCP} = U^{\theta_{\rm LP}}_{\rm Q,DC} = \frac{1}{\sqrt{2}} U_{\rm DC} \cdot (\cos\theta_{\rm LP} - {\rm i}\sin\theta_{\rm LP}) \ , \tag{15}$$

$$I_{{\rm Q},\theta_{\rm LP}} = \left|U^{\theta_{\rm LP}}_{\rm Q,Total}\right|^2 = \left|U^{\theta_{\rm LP}}_{\rm Q,LCP} + U^{\theta_{\rm LP}}_{\rm Q,DC}\right|^2 . \tag{16}$$

To assess the robustness of this interference scheme under non-ideal conditions ($\Gamma \neq \pi/2$), we simulated variations in the intensity ratio between the two interfering beams and examined their effect on the polarization state of the resulting field. The polarization state resulting from the interference between the object wavefront $U_{\rm LCP}$ with amplitude $\sqrt{\eta_{+1}}$ and the reference wavefront $U_{\rm DC}$, with amplitude $\sqrt{\eta_0}$, is expressed as:

$$\begin{aligned}&\sqrt{\eta_{+1}}{\rm e}^{+{\rm i}\Phi}\begin{pmatrix}1\\ -{\rm i}\end{pmatrix} + \sqrt{\eta_0}\begin{pmatrix}1\\ +{\rm i}\end{pmatrix} \\ &= \begin{pmatrix}\sqrt{\eta_0} + \sqrt{\eta_{+1}}{\rm e}^{{\rm i}\Phi} \\ {\rm i}\left(\sqrt{\eta_0} - \sqrt{\eta_{+1}}{\rm e}^{{\rm i}\Phi}\right)\end{pmatrix} .\end{aligned} \tag{17}$$

The polarization state of the resultant field is characterized by the ellipticity angle χ and the azimuth angle ψ, which are derived from the Stokes parameters:

$$\psi = \arctan\left(\frac{S_2}{S_1}\right) = \arctan\left(\frac{\sqrt{\eta_{+1}\eta_0}\sin\Phi}{\sqrt{\eta_{+1}\eta_0}\cos\Phi}\right) = \Phi \ , \tag{18}$$

$$\chi = \frac{1}{2}\arcsin\left(\frac{S_3}{S_0}\right) = \frac{1}{2}\arcsin\left(\frac{\eta_0 - \eta_{+1}}{\eta_0 + \eta_{+1}}\right) . \tag{19}$$

where S_0, S_1, S_2 and S_3 are the Stokes parameters representing the resultant polarization state. The total diffraction efficiency is conserved in the system, meaning the sum $\sqrt{\eta_{+1}} + \sqrt{\eta_0}$ is always ≤ 1. The ideal condition for dual-beam interference occurs when $\sqrt{\eta_{+1}} = \sqrt{\eta_0} = 0.5$, corresponding to perfectly balanced interfering amplitudes. Under this condition, the ellipticity angle χ becomes zero, indicating that the resulting polarization is purely linearly polarized. This linear polarization represents the optimal condition for phase encoding, ensuring maximum fringe contrast and minimal polarization distortion.

As the amplitude balance deviates from this ideal 1 ∶ 1 ratio, χ increases, and the polarization becomes elliptical. However, as shown in Fig. 3, while the ellipticity angle χ changes as the amplitude difference between $\sqrt{\eta_{+1}}$ and $\sqrt{\eta_0}$ varies, the azimuth angle ψ remains unaffected. This confirms that phase-encoded interference is preserved despite wavefront modulation efficiency imbalances. Consequently, the principal polarization axis, and thus the encoded phase information, is well preserved in the QWP-based GP-SIDH system. As a result, holographic reconstruction accuracy is maintained even in the presence of GP modulation efficiency dispersion. Additional simulation

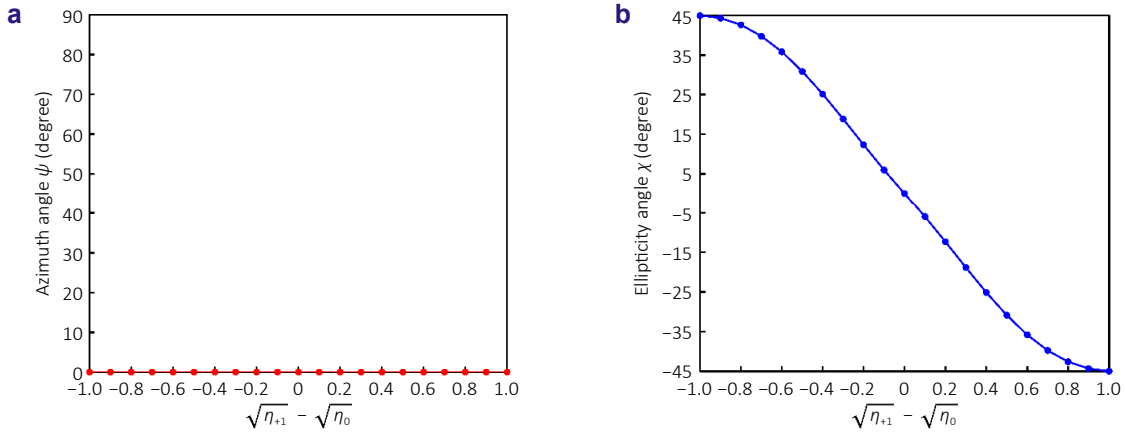


Fig. 3 | Simulated polarization characteristics of the interference between LCP and RCP beams. (a) Azimuth angle (ψ) and (b) ellipticity angle (χ) of the resulting polarization state were numerically calculated as functions of the amplitude ratio between the LCP and RCP components. While the ellipticity angle varies with the intensity ratio, the azimuth angle remains constant, indicating a stable polarization orientation despite amplitude imbalances.

results illustrating the evolution of the polarization state as a function of amplitude imbalance are provided in Fig. S1. This is crucial because, in four-phase shifting holography at GP-SIDH, accurate phase encoding—rather than the absolute polarization state—is essential for precise hologram reconstruction.

To accurately assess the performance of the GP lens and its impact on holographic reconstruction with SIDH under spectral variations, we modeled the wavelength-dependent wavefront modulation efficiency using Eq. (2), considering the wavelength-dependent material dispersion effects described by $\Delta n(\lambda) = n_e(\lambda) - n_o(\lambda)$. The refractive indices of the RM material RMM-141C (Merck, Germany) were measured as n_e = 1.732, 1.703, 1.688 and n_o = 1.553, 1.541, 1.535 at 450, 550, and 650 nm, respectively. These values were fit to the Cauchy equations:

$$n_e = 1.656 + \frac{1.203 \times 10^{-14}}{\lambda^2} + \frac{6.955 \times 10^{-28}}{\lambda^4}, \tag{20}$$

$$n_o = 1.523 + \frac{4.272 \times 10^{-15}}{\lambda^2} + \frac{3.735 \times 10^{-28}}{\lambda^4}. \tag{21}$$

Using these expressions along with Eqs. (2–4), the wavelength-dependent GP modulation efficiency was calculated and is shown in Fig. S2. Assuming the GP lens is optimized for 532 nm, the calculated 1st-order diffraction efficiencies for red (660 nm), green (532 nm), and blue (457 nm) are 84.93%, 100%, and 84.84% for the HWP-based configuration, and 30.69%, 50%, and 69.62% for the QWP-based configuration.

Simulations based on Eqs. (5–16) were performed in MATLAB (MathWorks, USA) using a Gaussian-distributed point source (500 μm diameter) as the object. Figure 4 presents a comparative analysis of RGB holographic reconstruction for both GP-SIDH systems. Under ideal, dispersion-free conditions (Fig. 4(b)), both HWP- and QWP-based configurations successfully reconstruct clean holographic images of the white point source. However, when wavelength-dependent dispersion is introduced (Fig. 4(c)), the HWP-based system exhibits significant ring-shaped noise in the red and blue channels due to residual 0th-order leakage and resulting triple-wavefront interference. This noise persists even after applying the four-phase shifting scheme during reconstruction. Channel-separated simulation results are provided in Fig. S3 for a more detailed comparison. In contrast, the QWP-based GP-SIDH system maintains artifact-free reconstructions across all RGB channels. Although the intensity ratio between the 0th- and ±1st-order beams varies with wavelength in the QWP configuration as well, the absence of a third interfering wavefront preserves stable two-beam polarization interference, enabling high-fidelity full-color holography.

To further evaluate the robustness of spatial phase encoding under realistic amplitude imbalances, additional simulations were performed using a convex lens phase profile with a 300 mm focal length. As shown in Fig. S4, the HWP-based system exhibits significant spatial variations in both azimuth and ellipticity angles due to triple-wavefront interference. In contrast, the QWP-based system reproduces an azimuth profile identical to the ideal two-beam case and shows only uniform ellipticity deviations. These findings underscore the superior resilience of the QWP-based GP-SIDH architecture in maintaining spatially encoded phase information integrity under broadband, non-ideal operating conditions.

2.3 Experimental demonstration of high-fidelity full-color imaging using QWP-based GP-SIDH

To experimentally validate the theoretical predictions, we implemented both HWP- and QWP-based GP-SIDH systems and evaluated their performance under broadband incoherent illumination. The GP lenses for both systems were fabricated with identical lens phase profiles and

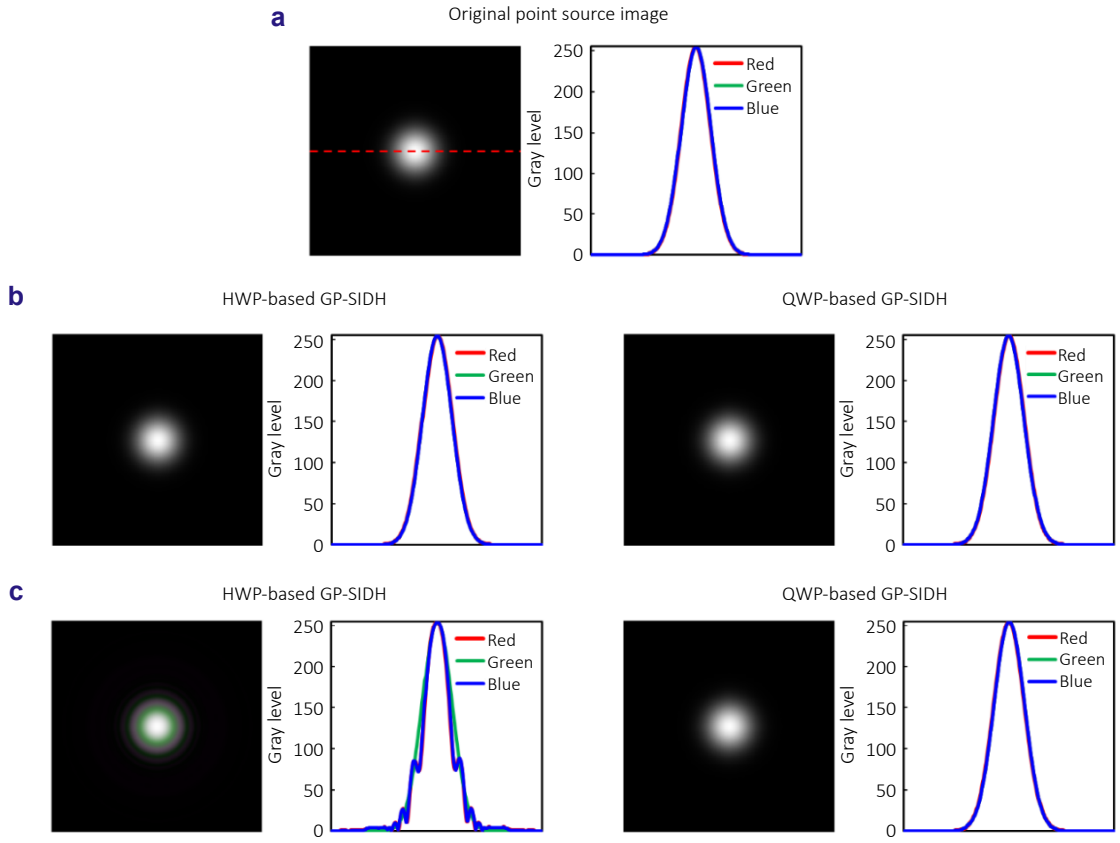


Fig. 4 | Simulated holographic image reconstruction for HWP-based and QWP-based GP-SIDH systems with a point source. (a) Intensity profile of the input point source used for reconstruction, along with the RGB channel cross-sectional profiles. (b) Reconstructed point-source images and corresponding intensity profiles for ideal HWP- and QWP-based systems, excluding wavelength-dependent variations in GP wavefront modulation efficiency. Both systems demonstrate spectrally balanced and artifact-free reconstructions under ideal achromatic conditions. (c) Reconstructed images and intensity profiles when wavelength-dependent wavefront modulation efficiency is considered. The HWP-based system exhibits noticeable spectral imbalance and ring-shaped noise artifacts in the red and blue channels due to residual 0^{th}-order wavefronts, while the QWP-based system maintains spectrally stable and noise-free reconstructions across all color channels.

examined under polarized optical microscopy (Fig. 5(a, b)). The experimental setups are shown in Fig. 5(c) and Fig. 5(d). In the HWP-based system, an LP was placed before the GP lens. In contrast, the QWP-based configuration incorporated an achromatic QWP between the LP and the GP lens to generate circularly polarized light at the input. This polarization state is essential for the QWP-based SIDH to function as designed, as the GP modulation relies on the accurate generation of LCP or RCP light. This configuration ensures the selective generation of only two self-interfering wavefronts, thereby enabling noise-free reconstruction.

Both systems were illuminated with a white LED source to support full-color imaging. As a test object, we used a multicolor target composed of three vertically aligned arrows, each dominated by red, blue, and green (RBG) spectral components rather than pure RGB primaries. This mixed-color design was chosen deliberately to assess the system's ability to resolve overlapping spectral content and highlight color crosstalk sensitivity under broadband conditions. A DSLR-acquired image of the object under the same illumination (Fig. 5(e)) served as the reference for evaluating reconstruction fidelity.

Four phase-shifted holograms were recorded simultaneously for each system using a pixel-divided, polarization-sensitive image sensor equipped with pixelized R/G/B color filters, as described in Fig. 1. The extracted complex holograms were numerically propagated to the object plane using wavelength-specific parameters to reconstruct RGB channels at a common focal depth. The results are shown in Fig. 5(f) for the HWP-based system and Fig. 5(g) for the QWP-based system.

The comparison clearly highlights the superior noise resilience of the QWP-based configuration. While the HWP-based reconstruction (Fig. 5(f)) successfully recovers the general arrow shapes and color layout, it suffers from significant background artifacts, particularly fringe-like interference and diffuse noise in the red and blue channels. These artifacts persist despite four-phase shifting and are

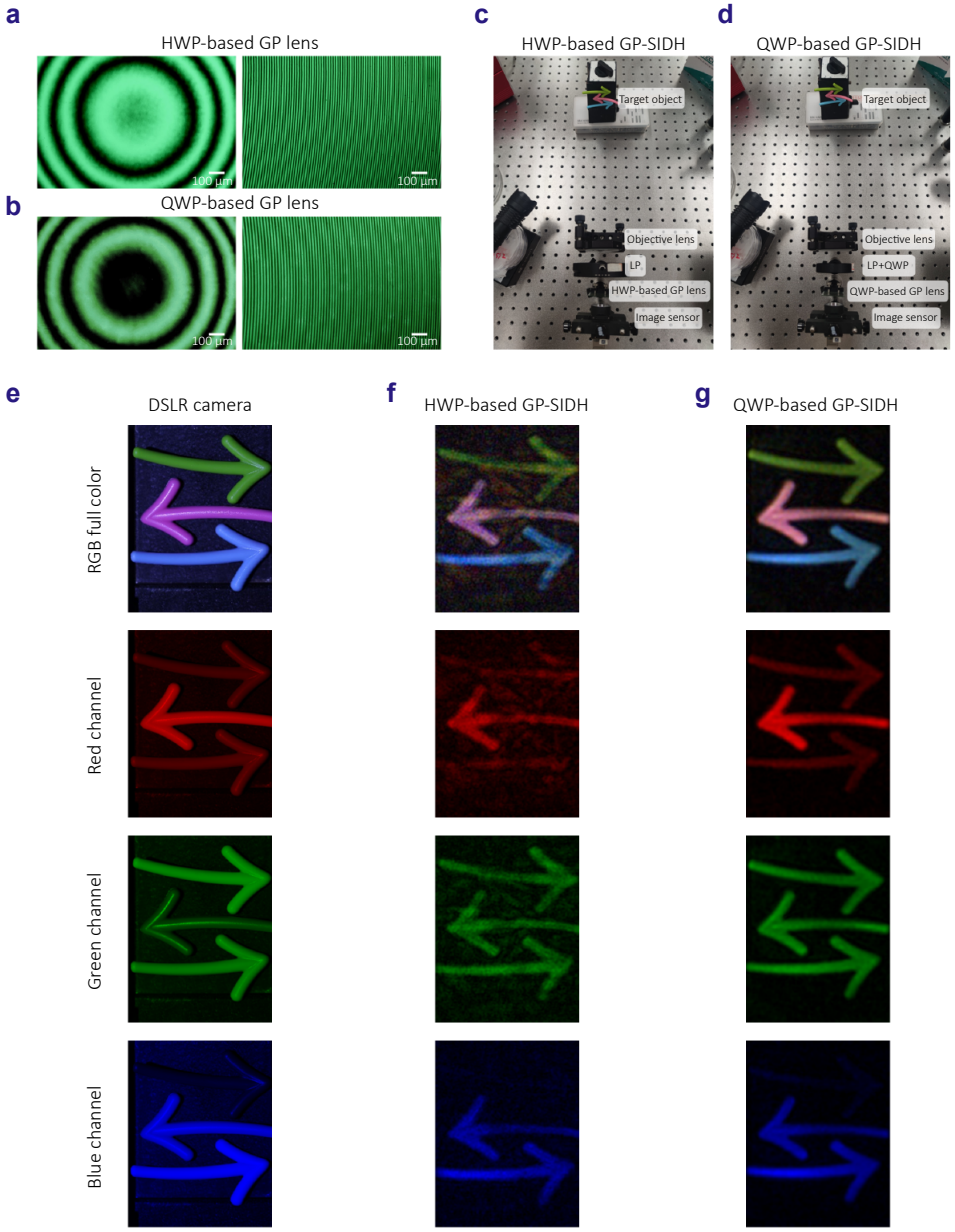


Fig. 5 | Experimental characterization and full-color holographic reconstruction results for GP-SIDH systems based on HWP- and QWP-based GP lenses. (a, b) Polarized optical microscope images of the fabricated GP lenses: (a) HWP-based and (b) QWP-based. In (a, b) uniformly uniaxial QWP was additionally inserted before the eyepiece to enhance phase contrast visualization. (c, d) Optical setups for the GP-SIDH systems: (c) HWP-based and (d) QWP-based configurations. Both setups use an LP; however, the QWP-based system includes an additional QWP between the LP and the GP lens. (e–g) RGB full-color and channel-separated images of the test object: (e) DSLR reference image, (f) holographic reconstruction using the HWP-based GP-SIDH, and (g) reconstruction using the QWP-based system. All reconstructions utilized the four-phase shifting method.

attributed to residual 0^{th}-order leakage resulting from triple-wavefront interference. By contrast, the QWP-based system (Fig. 5(g)) produces high-contrast, artifact-free reconstructions across all RGB channels. The resulting image closely matches the DSLR reference (Fig. 5(e)), demonstrating excellent fidelity in both spatial and color domains.

The measured spectral wavefront modulation efficiencies of the fabricated GP lenses are summarized in Table 1. The HWP-based lens shows near-ideal phase retardation in the blue spectral region, with modulation efficiency decreasing toward the red due to increasing retardation mismatch. Similarly, the QWP-based lens was optimized to achieve quarter-wave retardation primarily in the blue-to-green region, leading to the greatest amplitude imbalance in the red channel. However, as predicted by theory, this amplitude imbalance in the QWP-based configuration only affects

Table 1 | Measured GP wavefront modulation efficiencies of the fabricated HWP- and QWP-based GP lenses at red (660 nm), green (532 nm), and blue (457 nm) wavelengths. The table reports the ±1st- and 0th-order diffraction efficiencies for each configuration.

Wavelength (nm)	GP wavefront modulation efficiency (%)				
	HWP-based GP lens for LP			QWP-based GP lens for RCP	
	+1st order	−1st order	0th order	+1st order	0th order
660 (R)	36.65	36.65	26.7	30.0	70.0
532 (G)	46.65	46.65	6.7	42.0	58.0
457 (B)	49.55	49.55	0.9	59.4	40.6

the ellipticity of the polarization ellipses and does not degrade image quality. The four-phase shifting algorithm inherently suppresses spatially uniform ellipticity-induced noise, allowing the QWP-based system to maintain stable, artifact-free reconstructions across the entire RGB spectrum. As a result, it consistently outperforms the HWP-based system in visual quality.

To quantitatively evaluate reconstruction fidelity, SSIM maps were calculated for each color channel by comparing the reconstructed holograms to the DSLR reference. Figure 6(a) and 6(b) show the SSIM maps for the HWP-and QWP-based GP-SIDH systems, respectively. In these maps, brighter regions indicate higher local similarity to the reference image. The QWP-based system exhibits high and uniform SSIM values across all RGB channels, indicating strong local structural fidelity. In contrast, the HWP-based system displays pronounced SSIM degradation in the red and blue channels, particularly around the edges of the colored arrows, due to interference noise arising from residual 0th-order wavefronts. These localized degradations, caused by fringe-like artifacts, significantly reduce the average SSIM value in the HWP-based reconstruction, whereas the QWP-based result retains high and spatially uniform similarity, as summarized in Table 2. The difference is visually evident in Fig. 6(b), where the QWP-based map shows a more uniform and brighter similarity distribution. These results are supported by the quantitative PSNR and SSIM values in Table 2 (see also Supplementary information of Figs. S5 and S6 and Table S1 for results using a white dice object and RGB-separated analyses). The suppression of the unwanted third wavefront in the QWP-based design effectively eliminates triple-wavefront interference, improving color consistency and enabling noise-free, high-fidelity full-color holography under broadband incoherent illumination. The theoretical resolution limit of the current QWP-based GP-SIDH system is limited by the sensor Nyquist cutoff (equivalent to approximately 72.5 lp/mm at the sensor plane and approximately 1.6 lp/mm at the object plane) and the effective numerical aperture of the GP lens used, $NA_{\mathrm{eff}} = r_{\mathrm{h}}/z_{\mathrm{r}}$, where r_{h} denotes the hologram radius recorded on the sensor and z_r is the reconstruction distance. For the 400 mm focal length lens used in this study, the calculated object plane resolution limit is approximately 0.6–0.7 lp/mm. Experimental measurements using a USAF-1951 target yielded average CTF/MTF values of R 0.354/0.075, G 0.358/0.075, and B 0.441/0.061 with detailed measurement results presented in Table S2. The experimental setup for the measurement, the holographic phase angle data acquired through it, and the reconstruction results and ROI settings are as shown in Fig. S7. A dynamic validation of this experiment is also provided in Supplementary information of Movie S1, showing continuous holographic reconstruction while moving USAF-1951 target 1 under the same setup. This resolving power demonstrates that the current limitation arises from the chosen lens parameters rather than from the QWP-based approach itself, as adopting a shorter focal length (~150 mm) increases the NA_{eff}, bringing the achievable resolution closer to the Nyquist cutoff. Additionally, the present single-shot FoV is about 39° follows from r_{h}≈3.53 mm and z_{h}≈10 mm via $FoV = 2\arctan\left(r_{\mathrm{h}}/z_{\mathrm{h}}\right)$, where z_{h} denotes the separation between the GP lens and the image sensor. FoV can be increased by decreasing z_{h} at the usual trade-off with the effective numerical aperture $NA_{\mathrm{eff}} = r_{\mathrm{h}}/z_{\mathrm{r}}$ and object-plane resolution.

Having validated the improved reconstruction fidelity of the QWP-based GP-SIDH system for planar scenes, we next evaluated its ability to perform depth-resolved, full-color 3D imaging. In this experiment, two identical high-contrast objects—white dice with black dots—were used to assess the system's depth discrimination from a single hologram. The dice were chosen for their strong broadband reflectivity and textured surfaces, which provide useful features for evaluating reconstruction clarity across depth. As illustrated in Fig. 7(a), Dices 1 and 2 were placed along the optical axis with an axial separation of approximately 30 cm to ensure a meaningful depth interval. Both were illuminated simultaneously using a white LED source, and four phase-shifted holograms were captured in a single exposure using the QWP-based GP-SIDH setup described earlier. The resulting hologram encodes self-interference from both objects under incoherent illumination, made possible through polarization-selective modulation.

To reconstruct depth-resolved images, the extracted complex wavefront was numerically propagated to different axial planes. When focused on Dice 1 (Fig. 7(b)), the nearer object appears sharply resolved—its edges, spots, and color are clearly visible—while Dice 2 appears blurred and free of interference artifacts. The clean defocusing of Dice 2, without fringe contamination, demonstrates that the system

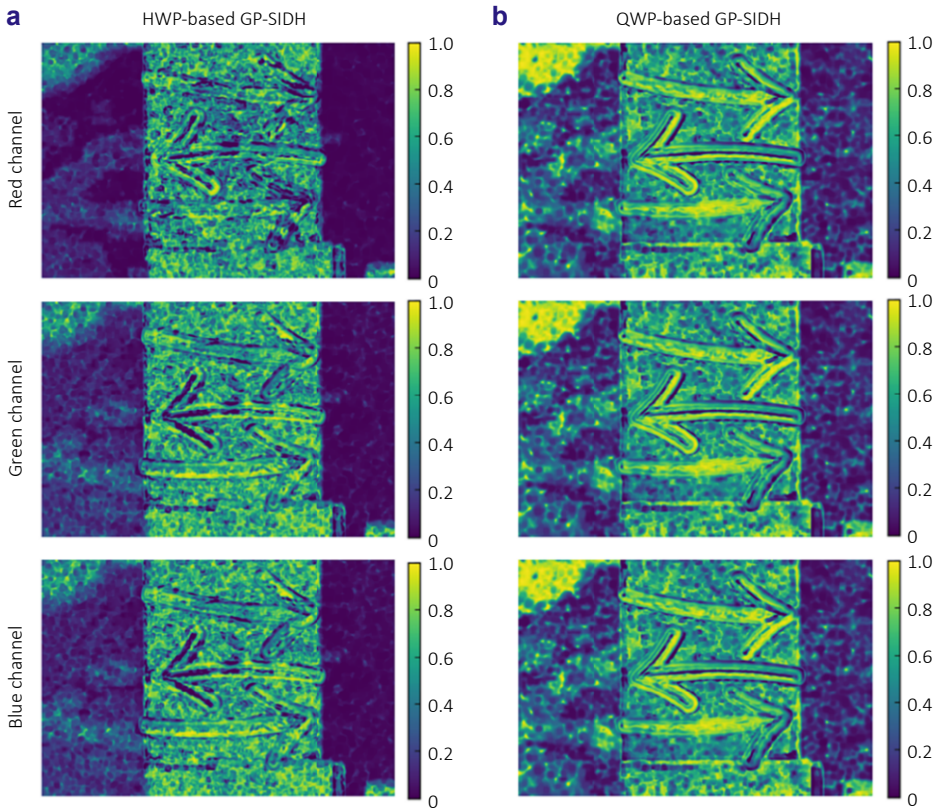


Fig. 6 | Structural similarity index (SSIM) maps comparing full-color holographic reconstructions with the DSLR reference image. (a) SSIM maps for the HWP-based GP-SIDH system, revealing significant similarity degradation in the red and blue channels due to interference-induced artifacts. (b) SSIM maps for the QWP-based GP-SIDH system, demonstrating consistently higher similarity across all RGB channels with minimal background noise. Brighter regions indicate greater local structural fidelity, confirming the QWP-based system's superior reconstruction performance.

Table 2 | Quantitative assessment of full-color holographic reconstructions using peak signal-to-noise ratio (PSNR) and SSIM metrics. Values were computed for each RGB channel by comparing the reconstructed images from the HWP- and QWP-based GP-SIDH systems (Fig. 5(f) and 5(g)) with the DSLR reference image (Fig. 5(e)).

Image channel	HWP-based GP-SIDH		QWP-based GP-SIDH	
	PSNR (dB)	SSIM	PSNR (dB)	SSIM
Red	17.88	0.265	19.89	0.397
Green	19.70	0.380	19.94	0.459
Blue	15.14	0.262	16.18	0.328

avoids coherence-induced crosstalk between depths. Upon refocusing to the plane of Dice 2 (Fig. 7(c)), it comes into sharp view while Dice 1 becomes defocused, further validating depth-specific imaging. This ability to switch focal planes digitally from a single-shot hologram highlights the system's true 3D imaging capability. Importantly, both reconstructions retain full-color fidelity, confirming that spectral content from each depth is preserved and accurately recovered under broadband incoherent illumination (see also Supplementary information of Movie S2 for dynamic refocusing). In addition, we provide a full-color holographic video acquired with the proposed QWP-based GP-SIDH (Supplementary information of Movie S3). This movie's result is presented without any post-processing, demonstrating that single-shot, video-rate full-color reconstructions can be reliably obtained with sufficiently low noise levels. Supplementary information of Movie S4 applies AI-based video super-resolution (VSR)[39] to the same sequence, further improving perceptual sharpness and smoothness and suggesting potential for field deployment. We also include Supplementary information of Movies S5 and S6, which show another scene with near- and far-depth holographic reconstruction: Supplementary information of Movie S5 is the raw reconstruction (no post-processing), and Supplementary information of Movie S6 is its VSR-enhanced counterpart, again corroborating the advantages

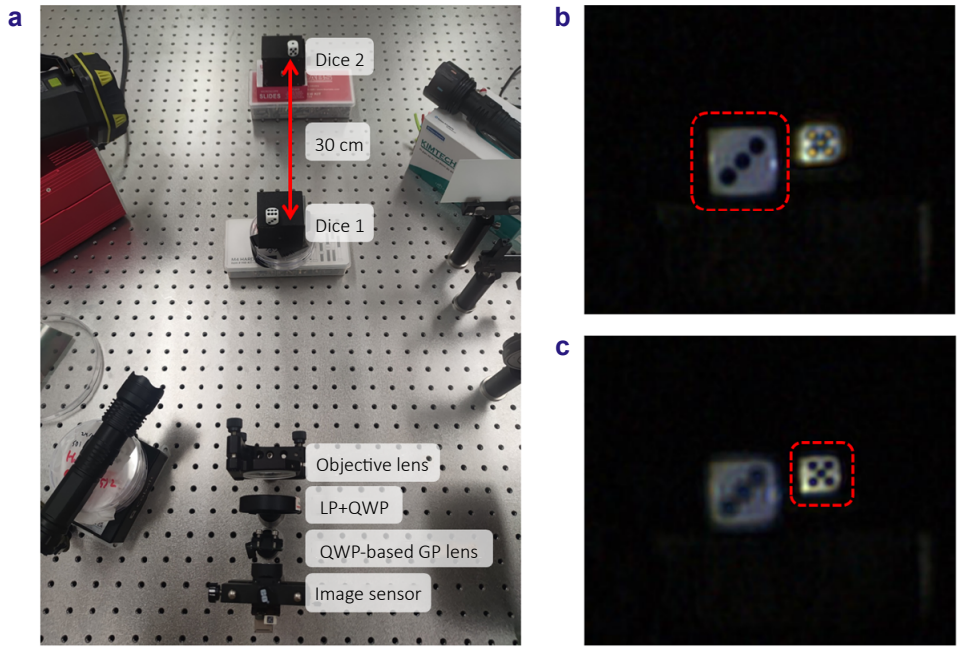


Fig. 7 | Depth-resolved full-color holographic reconstruction using the QWP-based GP-SIDH system. (a) Experimental setup showing two white dice (Dices 1 and 2) placed at different axial positions, separated by 30 cm. (b) Holographic reconstruction digitally refocused on Dice 1, revealing sharp surface details while Dice 2 appears blurred. (c) Reconstruction refocused on Dice 2, now clearly resolved as Dice 1 becomes defocused. These results demonstrate the system's capability for depth-selective, full-color holographic imaging under broadband incoherent illumination. See Supplementary information of Movie S2 for dynamic focal plane transitions.

of the proposed QWP-based GP-SIDH. Implementation details of the VSR workflow used for Supplementary information of Movies S4 and S6 are provided in the Supplementary information with Fig. S9. Because the proposed QWP-based GP-SIDH suppresses key noise sources at the optical acquisition stage, it remains compatible with a broad family of modern AI enhancement techniques that can be optionally applied to refine the final renderings further.

These results confirm that the QWP-based GP-SIDH system enables robust, multi-depth holographic imaging in incoherent lighting conditions. By effectively suppressing residual 0^{th}-order components, the system eliminates triple-wavefront interference, allowing each depth plane to be reconstructed independently with high spatial and color fidelity. This enables optical sectioning via numerical propagation, without the need for mechanical scanning or coherent sources. The successful imaging of both dice under white-light illumination further highlights the system's compatibility with real-world, broadband, non-coherent environments. In summary, the demonstrations presented in Figs. 5–7 validate the core advantages of the proposed design: the QWP-based GP lens architecture not only achieves artifact-free, full-color reconstructions but also extends SIDH capabilities to practical, high-fidelity 3D imaging applications —outperforming conventional HWP-based systems in both image quality and depth resolution.

3 Conclusion

3.1 Full-color SIDH imaging via QWP-based GP lens

The proposed QWP-based GP-SIDH configuration addresses the limitations of conventional HWP-based systems by structurally eliminating triple-wavefront interference. As demonstrated through theoretical modeling and confirmed by both simulations and experiments, the QWP design featuring a phase retardation of $\Gamma = \pi/2$, ensures that only two beams, the 0^{th}-order reference and a single $+1^{st}$ or -1^{st} -order object beam, interfere within the imaging system. When comparing light efficiency levels between conventional HWP-based GP-SIDH and the proposed QWP-based GP-SIDH system, both approaches generate orthogonal circularly polarized wavefront pairs for self-interference. The former achieves this under LP input conditions, whereas the latter proposed here utilizes a circularly polarized input state. Although the input polarization requirements differ, the proposed QWP-based configuration introduces no additional optical loss compared with the conventional HWP-based system. Importantly, the QWP-based GP-SIDH facilitates stable two-beam interference even under chromatic dispersion, enabling the QWP-based GP-SIDH to deliver high-fidelity, full-color reconstructions with minimal background noise and parasitic fringes. In contrast, HWP-based systems suffer from residual 0^{th}-order leakage and efficiency imbalances, especially across a broad spectral

range. Quantitative analyses further support these advantages, with consistently higher PSNR and SSIM values across all RGB channels, indicating superior structural similarity and color fidelity.

Beyond improving image quality, the QWP-based system streamlines the computational pipeline of digital holography. By eliminating the third interfering wavefront at the optical level, the recorded holograms capture only the object–reference interference component. This reduces the need for additional post-processing or noise suppression algorithms, enabling reliable amplitude and phase recovery using standard phase-shifting techniques. This simplification enhances computational efficiency and system reliability. These findings confirm the QWP-based GP-SIDH as a robust, scalable platform for full-color, incoherent digital holography[40]. Its resilience to wavelength-dependent variations in GP modulation efficiency, coupled with its streamlined optical and algorithmic design, makes it highly suitable for compact, broadband, and practical imaging applications. Furthermore, the results highlight the broader potential of polarization-sensitive GP optics to advance incoherent holographic imaging, particularly in applications requiring high color accuracy and system stability.

Looking ahead, this architecture could be extended to achieve higher spatial resolution by replacing the current pixel-divided polarization image sensor with a conventional high-resolution camera. Building on our previous work demonstrating temporal polarization switching in HWP-based SIDH[20], a similar approach could be applied to the QWP-based system by dynamically switching the incident circular polarization states. This would enable temporal multiplexing for phase-shift acquisition. However, further optimization is required in the design of circular polarization switching optics to embed phase information without introducing chromatic distortions. Special attention must be given to minimizing polarization-induced noise under broadband white-light illumination. Additionally, to maintain the key strengths of the GP-SIDH system, such as its compact form factor and video-capable acquisition, future research should focus on developing high-speed, integrated polarization switching elements[41–43]. These advancements will ultimately enable real-time, high-resolution, full-color 3D holography using QWP-based SIDH under incoherent illumination.

4 Materials and methods

4.1 Fabrication of GP Lenses

The GP lenses used in this study were fabricated by first spin-coating a photoalignment layer of Congo red (C0550, Tokyo Chemical Industry, Japan) onto glass substrates. The desired GP profile, corresponding to a lens with a 40 cm focal length, was then inscribed onto the alignment layer using a polarization interferometer. A RM solution (RMM-141C, Merck, Germany), dissolved in toluene, was spin-coated onto the patterned substrate to form the Pancharatnam–Berry phase film. For the HWP-based lens, the film thickness was adjusted to achieve a phase retardation of π at the design wavelength range of 457–532 nm, while the QWP-based lens was fabricated with a π/2 retardation. UV curing was performed under a nitrogen atmosphere to polymerize the birefringent RM layer. The completed GP lenses were characterized using polarized optical microscopy to verify the fidelity of the recorded phase profile and the uniformity of in-plane birefringence. Additionally, wavelength-dependent wavefront modulation efficiencies were measured using the optical setup shown in Fig. S8. The measured results agreed well with the theoretical values calculated from the birefringence dispersion model. The calculated efficiency values at RGB wavelengths are summarized in Table S3 in the supplementary information. Based on this consistency, HWP- and QWP-based GP lens samples were selected as fair and representative comparison controls in this study.

4.2 Optical setup for SIDH experiments

To enable a comparative analysis, two GP-SIDH systems were constructed: one using the conventional HWP-based GP lens and the other with the proposed QWP-based GP lens. In both setups, an LP was placed before the GP lens. In the QWP-based configuration, an achromatic QWP was additionally inserted between the LP and GP lens to generate an ideal circularly polarized incidence, which is crucial for suppressing triple-wavefront interference. In polarization-based SIDH systems, off-axis illumination can alter the effective retardation of the QWP and introduce ellipticity distortions in the wavefront modulations after the GP lens. In this experiment, such effects were minimized by restricting the operation to the central 12° of the system's total field of view (FoV) of approximately 39°. To further expand the FoV in future implementations, techniques such as synthetic aperture acquisition or multi-shot tiling/stitching —which enlarge the effective hologram area —may be incorporated into QWP-based GP-SIDH systems[44,45]. Moreover, the use of cholesteric liquid crystals (CLCs) has been reported as an effective method for mitigating polarization errors caused by off-axis illumination[46]. The achromatic QWP used in this configuration was a commercial CP42HE (Edmund Optics), which integrates an LP (XP42) with a QWP (WP140HE). The WP140HE provides a quarter-wave delay of 147 ± 4 nm at 560 nm, with an operating range from 450 nm to 650 nm. Its dispersion ratio is specified as R450/R550 = 0.90±0.03 and R650/R550 = 1.04±0.03. The reported retardation values were all obtained under normal-incidence conditions.

For full-color reconstruction, the test object consisted of a vertically aligned arrow target with red, green, and blue arrows, each composed of mixed primary color components to evaluate color fidelity across the visible spectrum. For

depth-resolved imaging, two white dice with black spots were placed along the optical axis, separated by approximately 30 cm to provide distinct axial planes. In both experiments, holograms were recorded using a pixelized polarization image sensor (PHX050S-QC, LUCID Vision Labs, Canada), which integrates a Sony IMX250MYR CMOS sensor. This sensor features a per-pixel wire-grid polarization filter array aligned at 0°, 45°, 90°, and 135°, directly overlaid on the standard Bayer color filter array (see Fig. 1). As a result, each 2 × 2 super-pixel block captures four polarization angles and three primary color channels, allowing single-shot acquisition of polarization-resolved full-color holograms. All experiments were conducted under spatially incoherent illumination using a broadband white-light LED source.

4.3 Numerical simulation of diffraction and reconstruction

To model wavefront behavior and holographic reconstruction, numerical simulations were performed in MATLAB (MathWorks, USA). The GP wavefront modulation efficiency of the GP lens was calculated based on the wavelength-dependent birefringence of the RM material, using experimentally measured refractive indices at 457 nm, 532 nm, and 660 nm. These values were fitted to the Cauchy equation to evaluate continuous spectral performance. Simulations were conducted with the following parameters: object-to-lens distance of 30 cm, lens-to-sensor distance of 2 cm, and a GP lens focal length of 15 cm. A Gaussian-distributed point source (diameter: 500 μm) was used to simulate hologram acquisition and RGB channel reconstruction. GP wavefront modulation efficiency and image fidelity were compared between the HWP-based and QWP-based GP-SIDH configurations, both under ideal and wavelength-dispersive conditions. The image sensor was modeled with a pixel size of 3.45 μm × 3.45 μm and a resolution of 2048 × 2048 pixels.

4.4 Image quality evaluation

The quality of the holographic images was quantitatively evaluated using the PSNR and SSIM metrics[47–50]. Reconstructed images for each RGB channel were compared against DSLR reference images captured under identical illumination conditions. SSIM maps were generated to visualize local structural fidelity, while PSNR values provided an overall measure of signal quality. These quantitative analyses confirm the superior performance of the QWP-based GP-SIDH system in suppressing reconstruction noise and preserving full-color fidelity across the visible spectrum.

In addition, the proposed QWP-based GP-SIDH system intrinsically reduces noise at the acquisition stage, thereby lowering the computational burden for post-processing. For a 1000 × 1000 RGB frame, a conservative estimate of the computational pipeline for QWP-based GP-SIDH —using only the Fresnel diffraction method (FDM) for holographic image reconstruction—requires approximately 20–35 MB of working memory and achieves a throughput of ~11–33 fps on a CPU (~67–200 fps on a GPU). By contrast, HWP-based GP-SIDH generally require an additional denoising step, such as Wiener filtering, which increases memory usage to ~40–60 MB and reduces throughput to ~4.5–11 fps on a CPU (~22–83 fps on a GPU). The techniques employed for noise reduction and their corresponding resource requirements are summarized in Table S4.

References

1. Kim J, Lee SJ. Digital in-line holographic microscopy for label-free identification and tracking of biological cells. *Mil Med Res* **11**, 38 (2024).
2. Lu ZZ, Cao YP, Liu M et al. Image-to-image translation for improved digital holographic reconstruction based on a generative adversarial network learning framework. *Opt Laser Technol* **166**, 109654 (2023).
3. Luo ZY, Li YNQ, Semmen J et al. Achromatic diffractive liquid-crystal optics for virtual reality displays. *Light Sci Appl* **12**, 230 (2023).
4. Gopakumar M, Lee GY, Choi S et al. Full-colour 3D holographic augmented-reality displays with metasurface waveguides. *Nature* **629**, 791–797 (2024).
5. Shin JY, Lee JW, Khaliq HS et al. Multi-depth switching by triple wavefront modulation of quarter-waveplate geometric phase lenses for vergence-accommodation-matching extended reality. *Light Sci Appl* **14**, 333 (2025).
6. Huang ZZ, Cao LC. Quantitative phase imaging based on holography: trends and new perspectives. *Light Sci Appl* **13**, 145 (2024).
7. Tahara T, Shimobaba T. Palm-sized single-shot full-color incoherent digital holographic camera system with white light. *Adv Devices Instrum* **6**, 0076 (2025).
8. Tian ZQ, Li LN, Ma JS et al. CFZA camera: a high-resolution lensless imaging technique based on compound Fresnel zone aperture. *Opt Lett* **49**, 3532–3535 (2024).
9. Lee KC, Bae J, Baek N et al. Design and single-shot fabrication of lensless cameras with arbitrary point spread functions. *Optica* **10**, 72–80 (2023).
10. Zhang X, Wang BW, Li S et al. Lensless imaging with a programmable Fresnel zone aperture. *Sci Adv* **11**, eadt3909 (2025).
11. Zheng SJ, Tan JR, Liu HJ et al. Orthogonal matrix of polarization combinations: concept and application to multichannel holographic recording. *Opto-Electron Adv* **7**, 230180 (2024).
12. Gao H, Fan XH, Wang YX et al. Multi-foci metalens for spectra and polarization ellipticity recognition and reconstruction. *Opto-Electron Sci* **2**, 220026 (2023).
13. Behal J, Memmolo P, Miccio L et al. On the optical performance of incoherent digital holography for extended 3D objects. *Opt Laser Technol* **170**, 110286 (2024).
14. Katz B, Rosen J, Kelner R et al. Enhanced resolution and throughput of Fresnel incoherent correlation holography (FINCH) using dual diffractive lenses on a spatial light modulator (SLM). *Opt Express* **20**, 9109–9121 (2012).
15. Liu JP, Tahara T, Hayasaki Y et al. Incoherent digital holography: a

review. *Appl Sci* **8**, 143 (2018).
16. Cohen E, Larocque H, Bouchard F et al. Geometric phase from Aharonov–Bohm to Pancharatnam–Berry and beyond. *Nat Rev Phys* **1**, 437–449 (2019).
17. Roux FS. Geometric phase lens. *J Opt Soc Am A* **23**, 476–482 (2006).
18. Choi K, Joo KI, Lee TH et al. Compact self-interference incoherent digital holographic camera system with real-time operation. *Opt Express* **27**, 4818–4833 (2019).
19. Choi K, Yim J, Min SW. Achromatic phase shifting self-interference incoherent digital holography using linear polarizer and geometric phase lens. *Opt Express* **26**, 16212–16225 (2018).
20. Choi K, Lee JW, Shin J et al. Real-time noise-free inline self-interference incoherent digital holography with temporal geometric phase multiplexing. *Photonics Res* **11**, 906–916 (2023).
21. Liang D, Zhang Q, Wang J et al. Single-shot Fresnel incoherent digital holography based on geometric phase lens. *J Mod Opt* **67**, 92–98 (2020).
22. Gopinath S, Bleahu A, Kahro T et al. Enhanced design of multiplexed coded masks for Fresnel incoherent correlation holography. *Sci Rep* **13**, 7390 (2023).
23. Rosen J, Alford S, Anand V et al. Roadmap on recent progress in FINCH technology. *J Imaging* **7**, 197 (2021).
24. Berry MV. Quantal phase factors accompanying adiabatic changes. *Proc Roy Soc A Math Phys Eng Sci* **392**, 45–57 (1984).
25. Huang YQ, Liu YC, Wang MW et al. Topological transition of Pancharatnam–Berry phase in a nonlocal twisted bilayer metasurface. *Sci Rep* **15**, 11182 (2025).
26. Bomzon Z, Biener G, Kleiner V et al. Space-variant Pancharatnam–Berry phase optical elements with computer-generated subwavelength gratings. *Opt Lett* **27**, 1141–1143 (2002).
27. Jisha CP, Nolte S, Alberucci A. Geometric phase in optics: from wavefront manipulation to waveguiding. *Laser Photonics Rev* **15**, 2100003 (2021).
28. Bomzon Z, Kleiner V, Hasman E. Pancharatnam–Berry phase in space-variant polarization-state manipulations with subwavelength gratings. *Opt Lett* **26**, 1424–1426 (2001).
29. Sakakura M, Lei YH, Wang L et al. Ultralow-loss geometric phase and polarization shaping by ultrafast laser writing in silica glass. *Light Sci Appl* **9**, 15 (2020).
30. Sugic D, Dennis MR, Nori F et al. Knotted polarizations and spin in three-dimensional polychromatic waves. *Phys Rev Res* **2**, 042045 (2020).
31. Shi Y, Lai YM, Liu YJ et al. Two-dimensional liquid crystal polarization grating via linearly polarized light modified multi-beam polarization interferometry. *Opt Express* **27**, 13061–13071 (2019).
32. Pal SK, Gangwar KK, Senthilkumaran P. Tailoring polarization singularity lattices by phase engineering of three-beam interference. *Optik* **255**, 168680 (2022).
33. Escuti MJ, Oh C, Sánchez C et al. Simplified spectropolarimetry using reactive mesogen polarization gratings. *Proc SPIE* **6302**, 630207 (2006).
34. Chen H, Lyu ZY, Wang CS. Tunable polarization holographic gratings obtained by varying the ratio of intensities of the recording beams. *Photonics Res* **12**, 749–754 (2024).
35. Nam SW, Moon S, Lee B et al. Aberration-corrected full-color holographic augmented reality near-eye display using a Pancharatnam-Berry phase lens. *Opt Express* **28**, 30836–30850 (2020).
36. Chen C, Gao SL, Xiao XJ et al. Highly efficient metasurface quarter-wave plate with wave front engineering. *Adv Photonics Res* **2**, 2000154 (2021).
37. Yamaguchi I. Phase-shifting digital holography. In Poon TC. *Digital Holography and Three-Dimensional Display: Principles and Applications* 145–171 (Springer, New York, 2006).
38. Zhang T, Yamaguchi I. Three-dimensional microscopy with phase-shifting digital holography. *Opt Lett* **23**, 1221–1223 (1998).
39. Choi K, Park D, Hong K. Full-color natural light holographic video camera. In *ACM SIGGRAPH 2025 Emerging Technologies* 6 (ACM, 2025). https://doi.org/10.1145/3721257.3734019.
40. Liu MZ, Zhu WQ, Huo PC et al. Multifunctional metasurfaces enabled by simultaneous and independent control of phase and amplitude for orthogonal polarization states. *Light Sci Appl* **10**, 107 (2021).
41. Kim HR, Lee YW, Kim SJ et al. A rotatable waveplate using a vertically aligned deformed-helix ferroelectric liquid crystal. *Ferroelectrics* **312**, 57–62 (2004).
42. Kim YH, Hur ST, Park CS et al. A vertical-field-driven polymer-stabilized blue phase liquid crystal mode to obtain a higher transmittance and lower driving voltage. *Opt Express* **19**, 17427–17438 (2011).
43. Joo KI, Park MK, Park H et al. Light-field camera for fast switching of time-sequential two-dimensional and three-dimensional image capturing at video rate. *IEEE Trans Ind Electron* **67**, 6975–6985 (2020).
44. Thurman ST, Bratcher A. Multiplexed synthetic-aperture digital holography. *Appl Opt* **54**, 559–568 (2015).
45. Pelagotti A, Paturzo M, Locatelli M et al. An automatic method for assembling a large synthetic aperture digital hologram. *Opt Express* **20**, 4830–4839 (2012).
46. Seo JH, Lee JW, Shin JY et al. Full-color holographic image capture: cholesteric liquid crystal circular polarizer combined with geometric phase lens reduces noise in self-interference incoherent digital holography. *J Soc Inf Disp* **33**, 553–565 (2025).
47. Dong ZX, Ling YY, Li Y et al. Motion Hologram: jointly optimized hologram generation and motion planning for photorealistic 3D displays via reinforcement learning. *Sci Adv* **11**, eads9876 (2025).
48. Yang D, Lee HS. Direct amplitude-only hologram realized by broken symmetry. *Sci Adv* **10**, eadp1205 (2024).
49. Chen G, Chen J, Liao HZ et al. Super-resolution reconstruction of off-axis digital holography based on Real-ESRGAN. *Appl Opt* **64**, 2245–2254 (2025).
50. Li ZS, Liu C, Li XW et al. Real-time holographic camera for obtaining real 3D scene hologram. *Light Sci Appl* **14**, 74 (2025).

Acknowledgements

This research was supported by the National Research Foundation (NRF) funded by the Korean government (MSIT) (No. RS-2024-00416272). This work was also supported by Electronics and Telecommunications Research Institute (ETRI) grant funded by ICT R&D program of MSIT/IITP [2019-0-00001, Development of Holo-TV Core Technologies for Hologram Media Services].

Author contributions

Hak-Rin Kim conceived the original idea, led and supervised the entire project, and revised the manuscript; Jae-Won Lee designed and conducted the experiments, established the optical configurations, analyzed the data, and drafted the manuscript (who has moved to new address: Reality Display Research Section, Electronics and Telecommunications Research Institute, Daejeon 34129, Republic of Korea); Jin-Hyeok Seo, Jung-Yeop Shin, and Jing-Wen Bu developed the fabrication process for the GP lenses, and performed their fabrication and characterization, and the related optical experiments; Kihong Choi and Keehoon Hong implemented and optimized the numerical algorithms for holographic reconstruction and contributed to data analysis.

Competing interests

The authors declare no competing financial interests.

Supplementary information

Supplementary information for this paper is available at https://doi.org/10.29026/oea.2026.250149

Open Access This article is licensed under a Creative Commons Attribution 4.0 International License, which permits use, sharing, adaptation, distribution and reproduction in any medium or format, as long as you give appropriate credit to the original author(s) and the source, provide a link to the Creative Commons license, and indicate if changes were made. To view a copy of this license, visit http://creativecommons.org/licenses/by/4.0/
©The Author(s) 2026.
Published by Editorial Office of *Opto-Electronic Advance*, Institute of Optics and Electronics, Chinese Academy of Sciences.

Opto-Electronic Journals Group
www.oejournal.org
Scan for Article PDF